Supplement of Hydrol. Earth Syst. Sci., 30, 1221–1245, 2026
https://doi.org/10.5194/hess-30-1221-2026-supplement

Hydrology and Earth System Sciences
Open Access
EGU

Supplement of

Modeling surface water and groundwater mixing and mixing-dependent denitrification with bedform dynamics

Xue Ping et al.

Correspondence to: Zhang Wen (wenz@cug.edu.cn)

List of supporting information:

S1: Criteria for ripple formation

S2: Model analysis and conservation calculation

S3: Model validation

S4: Sensitivity analysis of mixing process

S1: Criteria for ripple formation

In this study, ripples formation was qualitatively determined using the bedform stability diagram. This diagram is a summarized reference for examining equilibrium bed configurations in unidirectional flow, derived from a series of flume experiments and field studies (Ashley, 1990; Raudkivi, 1997). Besides, a series of quantitative criteria was developed to ensure ripple formation under the modeled scenarios and the achievement of dynamic equilibrium. Ripple development was assessed across different median particle size D_{50} and flow velocity conditions, in accordance with these quantitative criteria. Stream velocities (U) satisfying all these criteria were then selected (Fig. 3).

Ripples typically develop in low subcritical flow condition, in relatively shallow waters over sand riverbeds composed of fine to moderate sediment grains. The Froude number (Fr) of river should be smaller than the bedform threshold predictor (Ft). Ft indicates the beginning of the transition regime, marking the boundary for the occurrence of ripples and dunes (Karim, 1995; Zheng et al., 2019).

$$F_r = \frac{U}{\sqrt{gH}} \le F_t = 2.716\left(\frac{H}{D_{50}}\right)^{-0.25} \tag{S1}$$

where D_{50} [L] is the median grain size, H [L] is the water depth, and g [L T^{-2}] is the gravity acceleration.

According to Van Rijn's Shields diagram (van Rijn, 1984a, 1984b), ripples are present when the dimensionless particle diameter D^* is less than 10 and the shear velocity Reynolds number R_p does not exceed 11.6:

$$D^* = D_{50}\left(\frac{rg}{\upsilon^2}\right)^{1/3} < 10 \tag{S2}$$

$$R_p = \frac{u^* \cdot D_{50}}{\upsilon} \le 11.6 \tag{S3}$$

where r [-] denotes submerged specific gravity of sediment ($r = (\rho_s - \rho)/\rho$), υ [L^2 T^{-1}] represents kinematic viscosity of water. $u^* = (gHS)^{0.5}$ [L T^{-1}] is the bed shear velocity, S [-] is the stream gradient and calculated by Chezy equation ($U = H^{2/3}S^{1/2}/n$, where n [-] is the Manning coefficient and assumed to be 0.02 for sand).

The ripples begin to migrate as the bed shear velocity (u^*) exceeds the critical value (u_{cr}^*) for initiation of motion (van Rijn, 1984a, 1984b):

$$u^* > u_{cr}^* \tag{S4}$$

$$u_{cr}^* = \sqrt{\tau_{cr}/\rho} \tag{S5}$$

where u_{cr}^* [L T^{-1}] is the critical bed shear velocity and it can be calculated by the critical Shield parameter τ_{cr}^* ($\tau_{cr}^* = \tau_{cr} / g\,(\rho_s - \rho)\,D_{50}$). ρ_s [M L^{-3}] and ρ [M L^{-3}] are the density of sediment and water, respectively. The critical Shield parameter τ_{cr}^* represents the threshold for the initialization of motion, and it is determined by the dimensionless particle parameter D^* (Soulsby, 1997; Zheng et al., 2019):

$$\tau_{cr}^* = \frac{0.3}{1+1.2D^*} + 0.055\left[1 - \exp\left(-0.02D^*\right)\right] \tag{S6}$$

To sustain ripple migration in a state of dynamic equilibrium, conditions where the dimensionless particle diameter D^* is less than 10 and the transport stage parameter T is less than 3 must also be met (van Rijn, 1984a; 1984b). Here, T represents the mobility of sediment grains in terms of their movement stage relative to the critical stage required for the initiation of motion:

$$T = \frac{\left(u^*\right)^2 - \left(u_{cr}^*\right)^2}{\left(u_{cr}^*\right)^2} \tag{S7}$$

The ripples migration velocities are implemented using an empirical relation after Coleman and Melville (1994), which was derived from flume experiments:

$$\frac{u_c}{\left(u^* - u_{cr}^*\right)\left(\tau^* - \tau_{cr}^*\right)}\left(H_d/D_{50} - 3.5\right)^{1.3} = 40 \quad \text{(S8)}$$

where H_d [L] is the ripple height and u_c [L T^{-1}] represents ripple migration velocity.

Table S1. Parameters for bedform properties and hydraulic conditions used in this study

D_{50}	Re	U	D^*	T	S	$\tau_{cr}{}^*$	u^*	τ^*	$u_{cr}{}^*$	u_c
[mm]		[m s^{-1}]					[m s^{-1}]		[m s^{-1}]	[cm h^{-1}]
0.08	2000	0.100	2.037	-0.269	8.62E-5	0.089	0.0093	0.065	0.011	0
	2500	0.125	2.037	0.142	1.35E-4	0.089	0.0116	0.102	0.011	0.11
	3000	0.150	2.037	0.645	1.94E-4	0.089	0.0139	0.147	0.011	1.98
	3500	0.175	2.037	1.239	2.64E-4	0.089	0.0162	0.200	0.011	6.67
	4000	0.200	2.037	1.924	3.45E-4	0.089	0.0186	0.261	0.011	14.83
	4500	0.225	2.037	2.701	4.36E-4	0.089	0.0209	0.331	0.011	27.08
0.15	2500	0.125	3.819	-0.058	1.35E-4	0.058	0.0116	0.054	0.012	0
	3000	0.150	3.819	0.356	1.94E-4	0.058	0.0139	0.078	0.012	1.04
	3500	0.175	3.819	0.845	2.64E-4	0.058	0.0162	0.107	0.012	5.39
	4000	0.200	3.819	1.410	3.45E-4	0.058	0.0186	0.139	0.012	13.87
	4500	0.225	3.819	2.051	4.36E-4	0.058	0.0209	0.176	0.012	27.25
	5000	0.250	3.819	2.766	5.39E-4	0.058	0.0232	0.218	0.012	46.32
0.22	2500	0.125	5.601	-0.170	1.35E-4	0.045	0.0116	0.037	0.013	0
	3000	0.150	5.601	0.195	1.94E-4	0.045	0.0139	0.053	0.013	0.45
	3500	0.175	5.601	0.627	2.64E-4	0.045	0.0162	0.073	0.013	4.24
	4000	0.200	5.601	1.125	3.45E-4	0.045	0.0186	0.095	0.013	12.63
	4500	0.225	5.601	1.690	4.36E-4	0.045	0.0209	0.120	0.013	26.52
	5000	0.250	5.601	2.321	5.39E-4	0.045	0.0232	0.148	0.013	46.79
0.36	3000	0.150	9.165	-0.046	1.94E-4	0.034	0.0139	0.033	0.014	0
	3500	0.175	9.165	0.299	2.64E-4	0.034	0.0162	0.044	0.014	1.72
	4000	0.200	9.165	0.696	3.45E-4	0.034	0.0186	0.058	0.014	8.68
	4500	0.225	9.165	1.147	4.36E-4	0.034	0.0209	0.073	0.014	21.99

	5000	0.250	9.165	1.650	5.39E-4	0.034	0.0232	0.091	0.014	42.72
	5500	0.275	9.165	2.207	6.52E-4	0.034	0.0255	0.110	0.014	71.93
	6000	0.300	9.165	2.816	7.76E-4	0.034	0.0278	0.131	0.014	110.70

S2: Model analysis and conservation calculation

1) Comparison of single ripple with three consecutive ripples

The use of periodic boundaries at AB and DC is to replicate the repetitive geometric constraints of the riverbed. Simulations of three consecutive ripples were performed; particular attention was paid to the middle ripple, which was used to compare its vertical boundary pressure and solute concentration with results from the single-ripple model for conditions of Re = 3000, U_b = 0.6, and D_{50} = 0.15 mm. For the left boundary (AB), the single-ripple model exhibits a higher pressure compared to the three-consecutive-ripple model; in contrast, the single-ripple model has a lower pressure at the right boundary (CD). As a result, the pressure difference between these two vertical boundaries is greater in the single-ripple model (Fig. S1).

Furthermore, comparisons between the two models were carried out regarding simulated riverbed flow fields, nitrate plumes, fluxes, and reaction rates. The overall patterns of pressure, velocity, and solute distribution showed high similarity between the two models. We quantified the stream-/groundwater-borne nitrate influx and reaction rates within the riverbed. Minor differences were detected between these metrics (Table S2; < 5.00%). As a result, although moderate left/right boundary pressure differences were detected between their simulation results, such variations had negligible effects on reactive solute transport.

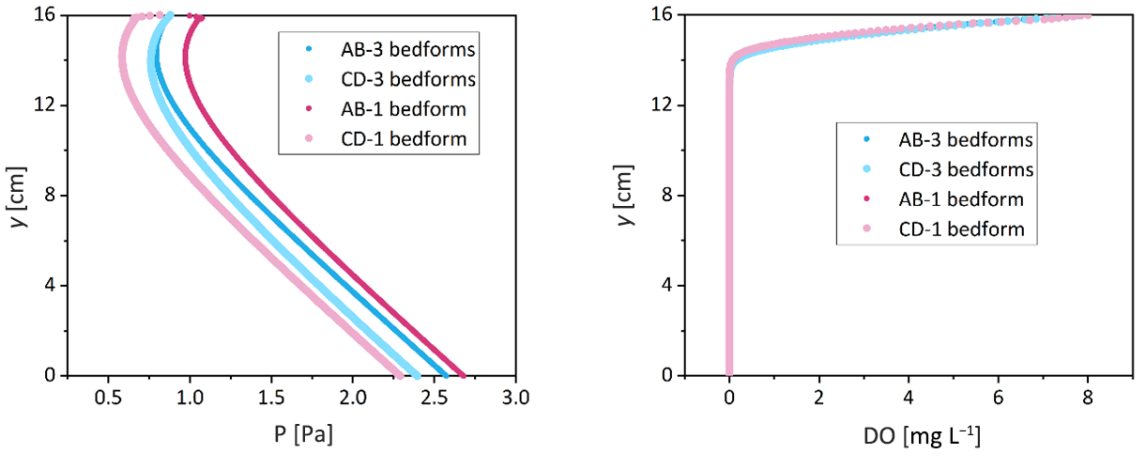

Figure S1. Comparison of pressure and oxygen concentration along the vertical boundaries between two models.

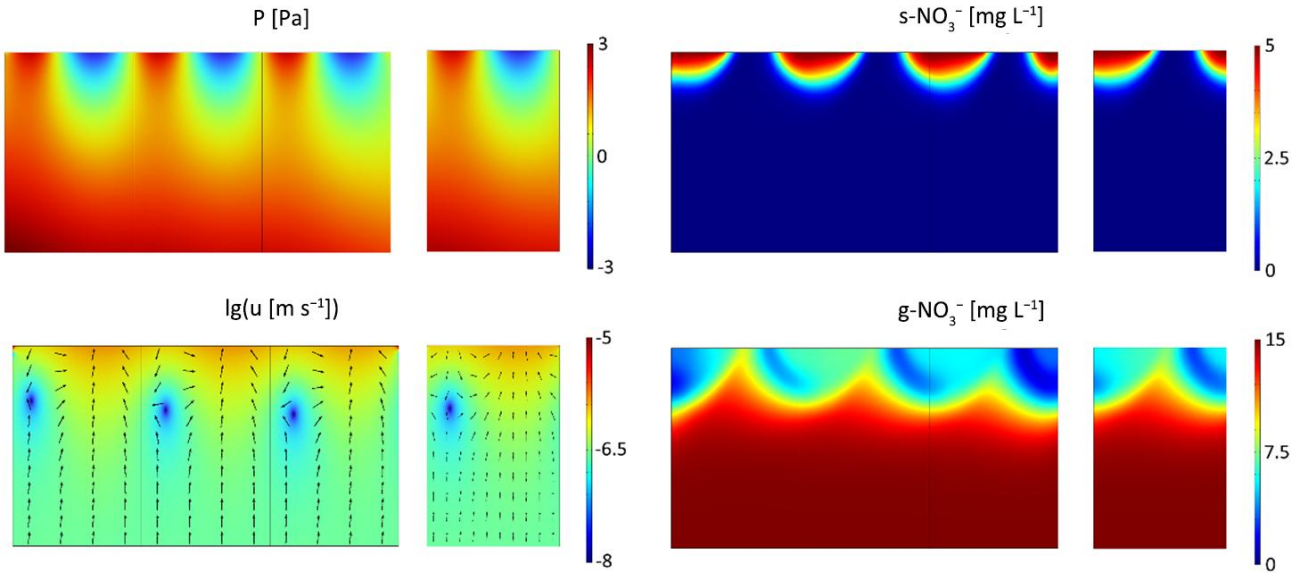

Figure S2. Comparison of pressure, Darcy velocity, stream-/groundwater- borne nitrate plumes between three-consecutive-ripple and single-ripple models.

Table S2. Comparison of stream-/groundwater- borne nitrate influx and reaction rate between three-consecutive-ripple and single-ripple models

Model metric	s_NO_3^- in [mg m^{-1} h^{-1}]	g_NO_3^- in [mg m^{-1} h^{-1}]	*R*s_NO_3^- [mg m^{-1} h^{-1}]	*R*g_NO_3^- [mg m^{-1} h^{-1}]
Three ripples	1.448	4.875	0.751	1.992
Single ripple	1.521	4.983	0.757	1.993
Error (%)	4.82	2.17	0.74	0.05

2) Model conservation calculation

Model conservation calculations were also performed to ensure fluid and solute mass balance. As an example, we verified the fluid and mass balance by calculating the total influx and outflow fluxes across all boundaries over the simulation period for conditions of Re = 3000, U_b = 0.6, and D_{50} = 0.15 mm. The mass conservation error for each time step of the transient model was calculated by strictly enforcing the solute mass balance, which accounts for inflow, outflow, reaction, and the mass accumulated within the computational domain. The time series of the mass conservation errors was presented in the following Fig. S3, where *x*-axis denotes passage ripple numbers and *y*-axis denotes

the magnitude of the mass conservation error. The errors exhibit a periodic pattern, which arises from the spatiotemporal variations in pressure head imposed on the top boundary of the simulated domain.

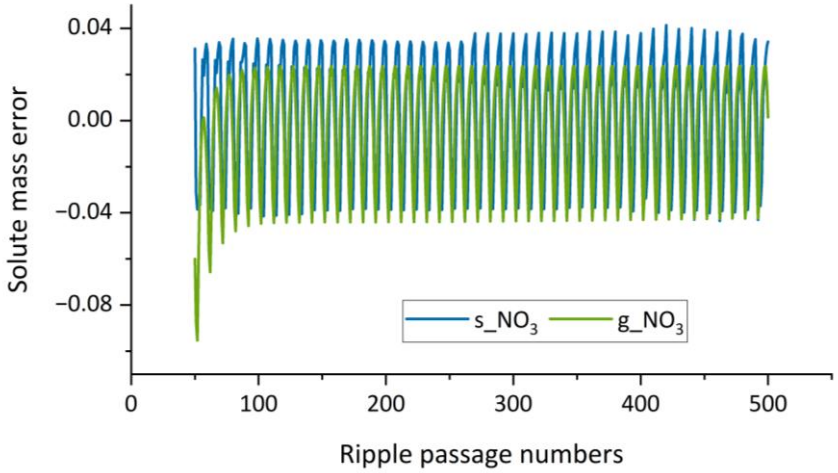

Figure S3. Mass conservation errors across different ripple passage numbers.

The fluid influx and outflux, as well as the solute input and output across various model boundaries, together with internal consumption were quantified and presented in the table below. Given the periodic characteristics of the conservation error, we calculated the average conservation errors over the entire simulation period (over 500 ripple passages). The influx of fluid is equal to the outflux of fluid. While the resulting conservation errors for stream- and groundwater-borne nitrate are 0.09% and 2.98%, respectively (Table S3).

Table S3. Model-calculated average conservation results over the entire stage

Boundary	fluid in [$m^2\ s^{-1}$]	fluid out [$m^2\ s^{-1}$]	$g\_NO_3^-$ in [$mg\ m^{-1}\ h^{-1}$]	$g\_NO_3^-$ out [$mg\ m^{-1}\ h^{-1}$]	$s\_NO_3^-$ in [$mg\ m^{-1}\ h^{-1}$]	$s\_NO_3^-$ out [$mg\ m^{-1}\ h^{-1}$]	$Rs\_NO_3^-$ [$mg\ m^{-1}\ h^{-1}$]	$Rg\_NO_3^-$ [$mg\ m^{-1}\ h^{-1}$]
BC (top)	6.16×10^{-8}	1.12×10^{-7}	1.247	1.928	1.305	0.547	0.756	1.908
AB (right)	7.87×10^{-9}	2.25×10^{-8}	0.189	0.693	0.045	0.177		
AB (left)	2.25×10^{-8}	7.86×10^{-9}	0.693	0.189	0.177	0.045		
AD (bottom)	5.04×10^{-8}	0.00	2.733	0.000	0.000	0.000		
Sum	1.42×10^{-7}	1.42×10^{-7}	4.862	2.809	1.527	0.770		
Error [%]	0		2.98		0.09			

Exactly, the initial mass balance error is larger due to the instantaneous changes in the initial conditions caused by the imposed boundary conditions. We calculated the conservation errors

between 400 and 500 ripple passages, the resulting conservation errors for stream- and groundwater-borne are 0.02% and 0.01%, respectively (Table S4). The solute influx is nearly equal to the sum of solute outflux and consumption. Notably, the relative error remains below the USGS threshold (less than 1%) for numerical models, effectively confirming the conservation of fluid and solute mass.

Table S4. Model-calculated average conservation results during the steady stage

Boundary	fluid in [$m^2\ s^{-1}$]	fluid out [$m^2\ s^{-1}$]	$g\_NO_3^-$ in [$mg\ m^{-1}\ h^{-1}$]	$g\_NO_3^-$ out [$mg\ m^{-1}\ h^{-1}$]	$s\_NO_3^-$ in [$mg\ m^{-1}\ h^{-1}$]	$s\_NO_3^-$ out [$mg\ m^{-1}\ h^{-1}$]	Rs_NO_3^- [$mg\ m^{-1}\ h^{-1}$]	Rg_NO_3^- [$mg\ m^{-1}\ h^{-1}$]
BC (top)	6.15×10^{-8}	1.12×10^{-7}	1.350	2.083	1.304	0.547	0.757	1.989
AB (right)	8.12×10^{-9}	2.23×10^{-8}	0.207	0.725	0.048	0.177		
AB (left)	2.23×10^{-8}	8.11×10^{-9}	0.725	0.207	0.176	0.048		
AD (bottom)	5.04×10^{-8}	0.00	2.722	0.000	0.000	0.000		
Sum	1.42×10^{-7}	1.42×10^{-7}	5.005	3.015	1.528	0.771		
Error [%]	0		0.01		0.02			

3) Grid independence analysis

Three computational grids were evaluated to ensure the simulated results independence of the grid resolution, confirming that the grid is sufficiently refined to capture mixing dynamics and minimize numerical dispersion. The grid sizes for the fine, base, and coarse grids were 1.5 mm, 2 mm, and 2.5 mm, respectively. We compared the critical model metrics, including hyporheic exchange flux, mixing flux, mixing area (i.e., the fraction of surface water ranges from 16% to 84%), nitrate influx, as well as denitrification rates (calculated equations referring to Sect. 2.6) calculated from varied grid models, using Re = 3000, U_b = 0.6, and D_{50} = 0.15 mm as an example. Calculated results were listed in Table S5. Simulated results showed negligible differences (less than 2%) among fine, base, and coarse grids; thus, the base grid size was selected, with the domain discretized into 19,940 cells.

Table S5. Model metrics calculated from coarse, base and fine grids

Grid size	Exchange flux [$m^2\ h^{-1}$]	Mixing flux [$m^2\ h^{-1}$]	Mixing size [cm^2]	$s\_NO_3^-$ in [$mg\ m^{-1}\ h^{-1}$]	$g\_NO_3^-$ in [$mg\ m^{-1}\ h^{-1}$]	Rs_NO_3^- [$mg\ m^{-1}\ h^{-1}$]	Rg_NO_3^- [$mg\ m^{-1}\ h^{-1}$]

Coarse	4.01×10^{-4}	1.67×10^{-4}	31.82	1.30	2.72	0.76	1.99
Base	4.02×10^{-4}	1.69×10^{-4}	32.19	1.30	2.72	0.76	1.99
Fine	4.05×10^{-4}	1.71×10^{-4}	32.64	1.31	2.72	0.76	1.99
Error 1 [%]	-0.45	-0.82	-1.14	0.30	0.00	-0.01	0.01
Error 2 [%]	-0.57	-1.43	-1.40	-1.03	0.00	0.00	0.00

Note: Error 1: Deviation of simulated results (coarse grid vs. base grid); Error 2: Deviation of simulated results (base grid vs. fine grid).

S3: Model validation

The flume experiments by Wolke et al. (2020) were conducted to investigate oxygen plume variation in homogeneous riverbeds under different conditions of stream velocity and bedform celerity conditions. We simulated flume experiments by Wolke et al. (2020) and compared the hyporheic exchange process and oxygen spatial distribution with experimental measurements to ensure the accuracy of numerical modeling. The experiment was designed with a total of 5 operating conditions, each of which was repeated twice and labeled as Set 1 and Set 2.

Table S6. Parameters for the flume experiments of Wolke et al. (2020)

Parameter	Description	Value
U [m s^{-1}]	Stream velocity	0.16−0.37
H_d [cm]	Bedform height	1.3−1.94
u_c [m h^{-1}]	Bedform celerity	0−0.699
H [cm]	Water depth	13.7−14.3
K [m s^{-1}]	Hydraulic conductivity	2.64×10^{-4}–4.64×10^{-4}
D_m [m^2 s^{-1}]	Molecular diffusion coefficient	5.0×10^{-9}
θ [-]	Porosity	0.36
D_{50} [mm]	Median grain size	0.264

α_L [m]	Longitudinal dispersivity	0.01
α_T [m]	Transverse dispersivity	0.001
K_O [mg L^{-1}]	Half-saturation constant for dissolved oxygen	4
c_O [mg L^{-1}]	Oxygen concentration in stream	7.36
V_O [h^{-1}]	Maximum rate of oxygen consumption	2

To evaluate both differences between the two models (i.e., flat bed model and triangular ripple model) and their reliability, two methods were employed to validate against the experimental data of Wolke et al. (2020). Note that the model parameters used in these two models were kept identical for each hydraulic condition. Comparisons of hyporheic exchange flux (HEF), oxygen influx (F_{in}), oxygen outflux (F_{out}), and oxygenated area (Ao), between the experimental data and the simulated results from the ripple bedform model and the flat bed model, were shown in Fig. 5 in Sect. 3.1.2.

Table S7. Hydraulic conditions of the flume experiments of Wolke et al. (2020)

Run	Set	U [m s^{-1}]	H_d [cm]	u_c [cm h^{-1}]	H [cm]
1	1	0.16	1.50	0	14.2
	2	0.16	1.94	0	14.2
2	1	0.25	1.13	0.035	13.8
	2	0.25	1.13	0.049	13.7
3	1	0.28	1.37	0.14	14.2
	2	0.29	1.37	0.135	13.9
4	1	0.32	1.38	0.394	14.2
	2	0.32	1.38	0.275	14.2
5	1	0.36	1.41	0.699	14.3
	2	0.37	1.41	0.644	13.8

S4: Sensitivity analysis of mixing process

No standard threshold governs surface water (SW) and groundwater (GW) mixing fractions, but mixing is generally recognized when GW proportion is 10%–90% (Hester et al., 2013; Woessner, 2000). To assess threshold impacts on mixing metrics, a sensitivity analysis tested three GW fraction

ranges: 10%–90%, 16%–84%, and 20%–80% (Fig. S4 and S5).

A wider GW fraction range results in a larger mixing flux, an elevated F_{mix}, and an expanded A_{mix}; however, the mixing zone remains a relatively thin layer (around 10–15% of the full domain) within the riverbed. Only slightly discrepancies in the computed F_{mix} and A_{mix} were found between the narrower range (20–80%) and the baseline range (16–84%). For various sediment grain sizes, the mixing flux represents approximately 60% of the total hyporheic exchange flux (HEF) in moderately to fast-moving bedforms, in contrast to roughly 20% in stationary and slow-moving bedforms. In the case of the wider range (10–90%), the mixing fraction makes up about 70% of the total HEF (a 10% increase relative to the other two ranges), and the mixing zone accounts for 15–20% of the whole riverbed (5% larger than the narrower and baseline ranges).

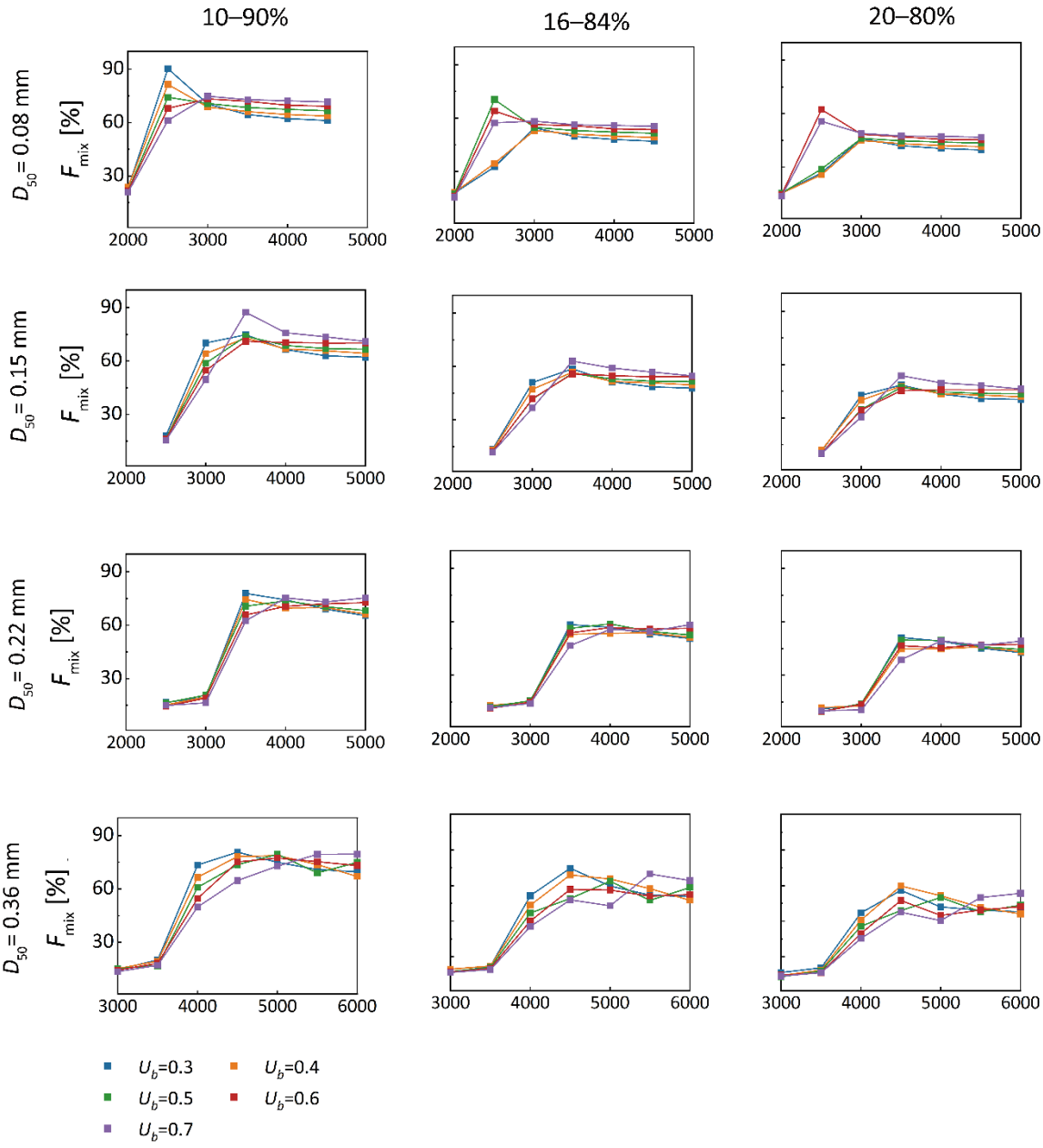

Figure S4. Variation in the proportion of mixing flux to hyporheic exchange flux (F_{mix}) as a function of *Re* across various medium sediment grain sizes and groundwater fraction ranges for U_b = 0.3−0.7.

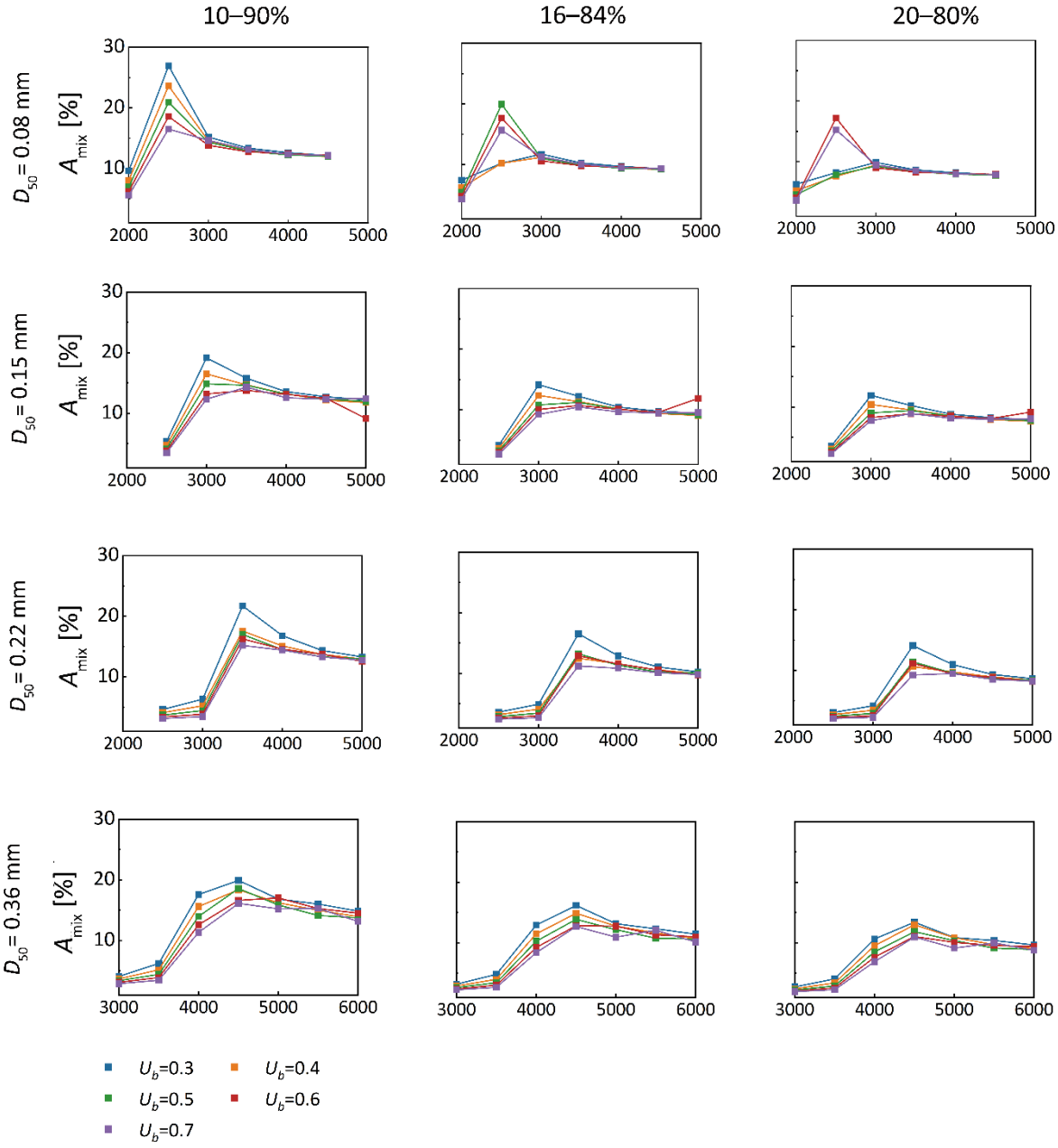

Figure S5. Variation in the proportion of mixing zone to the whole riverbed (A_{mix}) as a function of *Re* across various medium sediment grain sizes and groundwater fraction ranges for U_b = 0.3−0.7.

Longitudinal and transverse dispersivities (α_L and α_T) are important values for obtaining accurate mixing. Reported values of local dispersivities in the literature, and those used in previous modeling studies, fall within relatively narrow ranges despite some range of sediment textures. Here sensitivity analysis of local dispersivities was conducted by varying α_L from 0.001 to 0.015 m, with α_T set to1/10 of α_L. Taking a grain size of 0.15 mm and a constant ratio between pumping-driven

hyporheic exchange flux and upwelling groundwater flux (U_b = 0.6) as an example, we varied α_L from 0.001 to 0.015 m under different stream velocities (corresponding to four different *Re* numbers) and calculated the mixing fraction and mixing zone (Fig. S6). For the base case model, we set α_L equal to 0.001m and α_T equal to 0.0001m for groundwater borne conservation tracer.

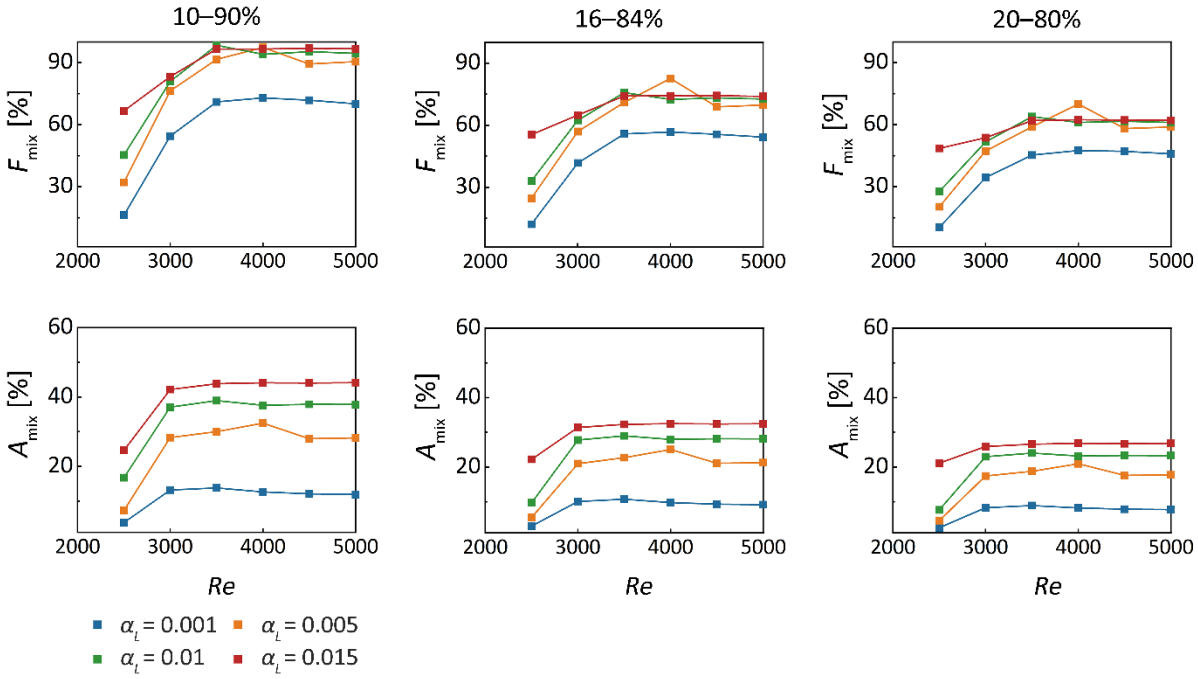

Figure S6. Variations in the ratio of mixing flux to hyporheic exchange flux (F_{mix}) and the ratio of mixing zone to the entire riverbed (A_{mix}) as functions of *Re* for different longitudinal dispersivities.

While larger longitudinal and transverse dispersivities significantly enhance F_{mix} and A_{mix}, they do not alter how bedform migration influences these mixing patterns. This confirms that increased dispersivities promotes greater mixing between groundwater and surface water, resulting in a higher proportion of hyporheic exchange flux contributing to mixing and a larger spatial extent of the mixing zone. To accurately estimate the magnitude of mixing, it is important to obtain reliable estimates of dispersion parameters.

References

Ashley, G. M. (1990). Classification of large-scale subaqueous bedforms: A new look at an old problem-SEPM bedforms and bedding structures. Journal of Sedimentary Research, 60(1), 160–172. https://doi.org/10.1306/212F9138-2B24-11D7-8648000102C1865D

Hester, E. T., Young, K. I., and Widdowson, M. A. (2013). Mixing of surface and groundwater induced by riverbed dunes: Implications for hyporheic zone definitions and pollutant reactions. Water Resources Research, 49, 5221–5237. https://doi.org/10.1002/wrcr.20399.

Raudkivi, A. J. (1997). Ripples on stream bed. Journal of Hydraulic Engineering, 123(1), 58–64. https://doi.org/10.1061/(ASCE)0733-9429(1997)123:1(58)

Karim, F. (1995). Bed configuration and hydraulic resistance in alluvial-channel flows. Journal of Hydraulic Engineering, 121(1), 15–25. https://doi.org/10.1061/(ASCE)0733-9429

Soulsby, R. (1997). Dynamics of marine sands: a manual for practical applications. Oceanographic Literature Review, 9, 947.

van Rijn, L. C. (1984a). Sediment transport: Part I–Bed load transport. Journal of Hydraulic Engineering, 110(12), 1733–1754. https://doi.org/10.1061/(ASCE)0733-9429

van Rijn, L. C. (1984b). Sediment transport: Part III–Bed forms and alluvial roughness. Journal of Hydraulic Engineering, 110(10), 1431–1456. https://doi.org/10.1061/(ASCE)07339429

Woessner, W. (2000). Stream and fluvial plain ground water interactions: rescaling hydrogeologic thought. Ground Water, 38(3), 423–429. https://doi.org/10.1111/j.1745-6584.2000.tb00228.x

Wolke, P., Teitelbaum, Y., Deng, C., Lewandowski, J., and Arnon, S. (2020). Impact of bed form celerity on oxygen dynamics in the hyporheic zone. Water, 12(1), 62. https://doi.org/10.3390/w12010062

Zheng, L., Cardenas, M. B., Wang, L., and Mohrig, D. (2019). Ripple effects: Bed form morphodynamics cascading into hyporheic zone biogeochemistry. Water Resources Research, 55, 7320–7342. https://doi.org/10.1029/2018WR023517